

# Modeling, Inference, and Prediction in Mobility-Based Compartmental Models for Epidemiology

Ning Jiang\*, Weiqi Chu\*, Yao Li\*

## Abstract

Classical compartmental models in epidemiology often struggle to accurately capture real-world dynamics due to their inability to address the inherent heterogeneity of populations. In this paper, we introduce a novel approach that incorporates heterogeneity through a mobility variable, transforming the traditional ODE system into a system of integro-differential equations that describe the dynamics of population densities across different compartments. Our results show that, for the same basic reproduction number, our mobility-based model predicts a smaller final pandemic size compared to classic compartmental models, whose population densities are represented as Dirac delta functions in our density-based framework. This addresses the overestimation issue common in many classical models. Additionally, we demonstrate that the time series of the infected population is sufficient to uniquely identify the mobility distribution. We reconstruct this distribution using a machine-learning-based framework, providing both theoretical and algorithmic support to effectively constrain the mobility-based model with real-world data.

## 1 Introduction

Understanding and predicting epidemic dynamics are crucial for public health planning and response [9, 14, 16]. Accurate models facilitate the timely implementation of control measures, resource allocation, and strategy development, which are essential for minimizing the impact of infectious diseases. For instance, during the COVID-19 pandemic, models by Ferguson et al. [7] guided decisions on lockdowns and social distancing, significantly influencing policy and saving lives.

Compartmental models have been a cornerstone in epidemiology since the early 20th century. These models, such as the classic SIR (Susceptible-Infected-Recovered) model introduced by Kermack and McKendrick [11], divide the population into compartments based on disease status. The transitions between compartments are governed by differential equations that describe the dynamics of disease transmission and recovery. These models have been instrumental in understanding various infectious diseases, including influenza, measles, and more recently, COVID-19. Compartmental models provide a simplified yet powerful framework to study the spread of diseases within a population.

Traditional compartmental models, despite their utility, face significant limitations [1, 10]. One major constraint lies in their assumption of a homogeneous mixing population, where every individual has an equal probability of coming into contact with any other individual, disregarding the complex realities of social interactions and geographic distributions [2, 15]. Furthermore, these models typically omit spatial dynamics, which is critical for understanding disease spread across different regions and the localized impact of interventions [6]. Additionally, traditional models often fail to account for dynamic changes in human behavior during epidemics, such as increased handwashing, social distancing, and vaccination uptake, which can profoundly influence epidemic outcomes [5, 8]. This oversimplification neglects the diverse patterns of human contact within communities.

---

\*Department of Mathematics and Statistics, University of Massachusetts Amherst, Amherst, Massachusetts, the United States, 01003

The current ODE-based epidemiological models frequently overestimate pandemic size by assuming homogeneous mixing and neglecting real-world contact patterns [3, 12, 13]. Moreover, the classic models often fail to incorporate behavioral changes such as increased hygiene practices or timely interventions, which can inflate estimates of susceptible populations and contribute to the overall overestimation. To address these issues, we propose mobility-based compartmental models where the population exhibits heterogeneous mobility distributions. Individuals with higher mobility are at increased risk of infection and transmission during the early stages of the pandemic, potentially leading to a higher basic reproduction number ( $\mathcal{R}_0$ ) initially. However, as the pandemic progresses, the initially infected high-mobility group recovers and subsequently provides indirect protection to the low-mobility group, thereby reducing  $\mathcal{R}_0$  and ultimately limiting the pandemic size. This mobility-based infection mechanism offers a straightforward yet effective approach to more accurately estimate pandemic spread, addressing the overestimation observed in traditional compartmental models used in epidemiology.

Our paper proceeds as follows. In section 2, we propose a mobility-based heterogeneous compartmental model, highlighting its distinctions from homogeneous models in terms of  $\mathcal{R}_0$  and the final pandemic size. In section 3, we present an inverse problem aimed at inferring the mobility distribution from the time series of the infected population. We provide sufficient conditions to infer the mobility distribution uniquely and propose a machine-learning approach for inferring the mobility distribution. We conclude in section 4.

## 2 Model description and properties

### 2.1 A mobility-based SIRS model

The baseline SIRS model delineates infectious disease dynamics within a population, categorizing individuals into susceptible (S), infected (I), and recovered (R) compartments. Consider a system with  $N$  agents, in which agent  $i$  holds a state  $X_i$  that takes a value S, I, or R. We define  $S(t)$ ,  $I(t)$ , and  $R(t)$  as the ratios of agents in the three states as

$$S(t) = \frac{1}{N} \sum_{i=1}^N \mathbf{1}_{\{X_i(t)=S\}}, \quad I(t) = \frac{1}{N} \sum_{i=1}^N \mathbf{1}_{\{X_i(t)=I\}}, \quad R(t) = \frac{1}{N} \sum_{i=1}^N \mathbf{1}_{\{X_i(t)=R\}}. \quad (1)$$

The baseline SIRS model posits that individuals transition cyclically between S, I, and R states through infection, recovery, and subsequent loss of immunity, all modeled as independent Poisson-point processes with constant rates. The well-known SIRS model describes the population dynamics of the three compartments as

$$\begin{aligned} \dot{S}(t) &= -\beta S(t)I(t) + \varepsilon R(t) \\ \dot{I}(t) &= \beta S(t)I(t) - \gamma I(t) \\ \dot{R}(t) &= \gamma I(t) - \varepsilon R(t), \end{aligned} \quad (2)$$

where  $\beta$  is the infection rate,  $\gamma$  is the recovery rate, and  $\varepsilon$  is the loss of immunity rate.

However, this baseline model overlooks the heterogeneity among individuals within a population, which is critical for understanding disease transmission. Among various factors, mobility plays a pivotal role in epidemics by accelerating infection movement across regions through travel, commuting, and migration. We propose a mobility-based SIRS model where each agent  $i$  has a time-independent mobility  $m_i \in (0, 1)$  that determines the infection and transmission rates of agent  $i$ . All S-I pairs (e.g., a pair of agents  $i$  and  $j$  with  $X_i = S$  and  $X_j = I$ ) are subject to internal infections, with the probability of agent  $j$  infecting agent  $i$  given by  $\beta m_i m_j$ . Infected agents recover at a constant rate  $\gamma$ , and recovered agents lose immunity at a constant rate  $\varepsilon$ , consistent with the baseline model (2). Figure 1 illustrates the transitions between the three compartments and their respective rates.

We describe the dynamics using three population density functions of mobility— $S(m, t)$ ,  $I(m, t)$ ,  $R(m, t)$ —associated with the susceptible, infected, and recovered compartments, respectively. Here,

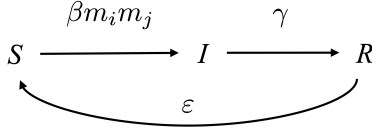


Figure 1: A schematic diagram to show the transition between three compartments and the transition rates in the mobility-based compartments models.

$S(m, t)dm$ , represents the ratio of susceptible agents with mobility in the interval  $[m, m + dm, )$ . Due to population conservation, we have

$$S(m, t) + I(m, t) + R(m, t) = f(m), \quad \text{for all } t \geq 0, \quad (3)$$

where  $f(m)$  denotes the time-independent mobility distribution function. The corresponding mobility-based SIRS model is

$$\frac{\partial}{\partial t} S(m, t) = -\beta \int_0^1 mm' S(m, t) I(m', t) dm' + \varepsilon R(m, t) \quad (4a)$$

$$\frac{\partial}{\partial t} I(m, t) = \beta \int_0^1 mm' S(m, t) I(m', t) dm' - \gamma I(m, t) \quad (4b)$$

$$\frac{\partial}{\partial t} R(m, t) = \gamma I(m, t) - \varepsilon R(m, t). \quad (4c)$$

In the mobility-based SIRS model, a susceptible agent with mobility  $m$  can be infected by any infected agent with mobility  $m'$ , leading to an integral representation of the internal infection process. In our model, each agent's mobility is time-independent, resulting in local terms for the recovery and loss of immunity processes.

If all agents have the same mobility  $m_0$ , then the mobility distribution is a Dirac delta function centered at  $m_0$  (i.e.,  $f(m) = \delta(m - m_0)$ ). The mobility-based SIRS model (4) becomes the baseline SIRS model (2) with the infection rate  $\beta_{\text{eff}} = \beta m_0^2$ , where we refer  $\beta_{\text{eff}}$  to as the effective infection rate.

## 2.2 Dynamics of the mobility-based SIRS model

In Figure 2, we illustrate the time evolution of the three population densities in the mobility-based SIRS model (4) during the first infection wave. Initially, the population is evenly distributed across the mobility domain  $[0, 1]$ . As the simulation begins, susceptible agents with high mobility are infected first, leading to a peak in the infected population density near  $m = 1$  at  $t = 250$ . Over time, the infected population recovers, resulting in an increased density in  $R(m, t)$ . This infection-recovery process occurs earlier in the high-mobility region compared to the low-mobility region.

The initial mobility distribution plays a crucial role in determining the mobility heterogeneity of the population as well as shaping the aggregated dynamics. We define the short-hand notation for the integral

$$\langle g \rangle(t) := \int_0^1 g(m, t) dm, \quad (5)$$

and illustrate the time evolution of the ratios of three compartments in Figure 3. We fix the second-order moment of the initial mobility distribution (i.e.,  $\langle m^2 f \rangle$ ) in all simulations, which, as we will show in section 2.3, is proportional to the basic reproduction number  $\mathcal{R}_0$ . In addition, we use the initial conditions

$$S(m, 0) = (1 - I_0)f(m), \quad I(m, 0) = I_0f(m), \quad R(m, 0) = 0, \quad (6)$$

which we refer to as the proportional initial condition. We will use this initial condition by default without further explanation. We choose three initial mobility distributions that all have the same

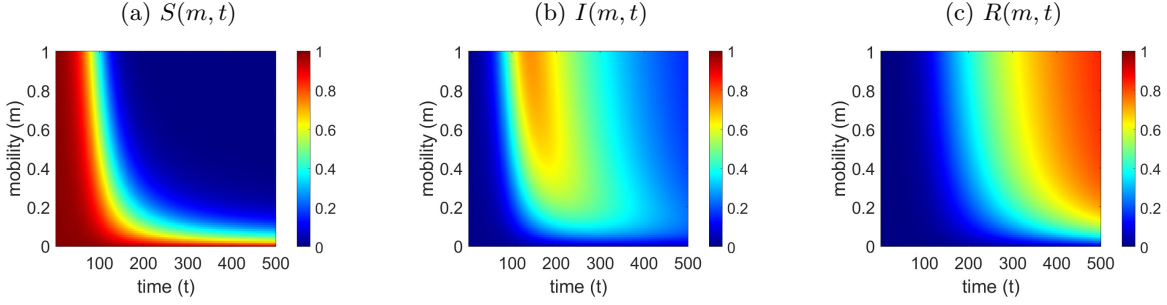


Figure 2: Evolution dynamics of the mobility-based SIRS model (3), with parameter  $\beta = 0.1, \varepsilon = 0.01, \gamma = 0.3$  and initial  $S(m, 0) = 0.99, I(m, 0) = 0.01, R(m, 0) = 0$ , for (a) the susceptible population  $S(m, t)$ , (b) the infected population  $I(m, t)$ , and (c) the recovered population  $R(m, t)$ .

second-order moment  $\langle m^2 f \rangle$ , where  $f_1$  and  $f_2$  are restricted normal distributions on  $[0, 1]$  with

$$f_1 \propto 0.8\mathcal{N}(0.1, 0.02) + 0.2\mathcal{N}(0.95, 0.02), \quad f_2 \propto \mathcal{N}(0.2, 0.365), \quad (7)$$

and  $f_3$  is a Direct delta function  $f(m) = \delta(m - 0.435)$ .

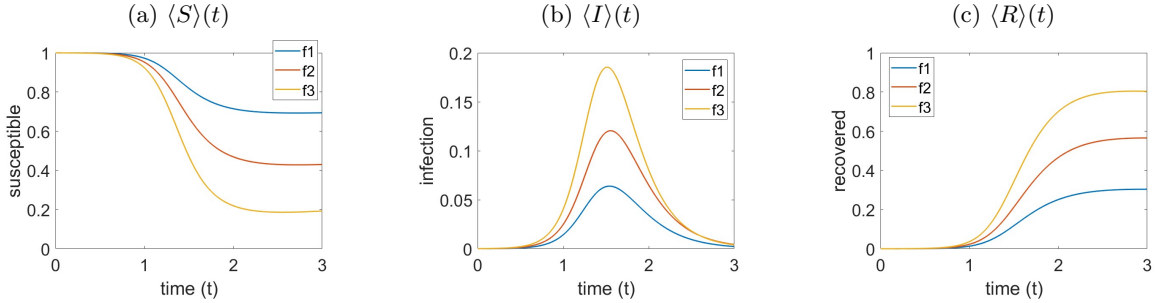


Figure 3: Time evolution of the ratios of three compartments in the mobility-based SIRS model (3), with parameters  $\beta = 1.5, \gamma = 0.13, \varepsilon = 0.001$  and the proportional initial condition with  $I_0 = 1e-4$  in (6).

### 2.3 Basic reproduction number

The basic reproduction number  $\mathcal{R}_0$  is a key epidemiological metric that represents the average number of secondary infections produced by a single infected individual in a fully susceptible population. In this section, we derive  $\mathcal{R}_0$  of the mobility-based SIRS model (4).

We consider the next-generation matrix method [4] and discretize  $I(m, t)$  and  $S(m, t)$  on the grids  $\{m_i\}_{i=1}^M$ . We denote the discretized quantities by two vectors  $\mathbf{x}, \mathbf{y} \in \mathbb{R}^M$ , in which

$$x_i(t) = I(m_i, t), \quad y_i(t) = S(m_i, t). \quad (8)$$

We consider a numerical quadrature to replace the integral in (4) with

$$\int_0^1 m' I(m', t) dm' \approx \sum_{i=1}^M w_i m_i x_i, \quad (9)$$

where  $w_i$  is the weight of the numerical quadrature at the grid point  $m_i$ . We write (4) in a discrete format and obtain

$$\dot{\mathbf{x}} = \mathbf{F}(\mathbf{x}, \mathbf{y}) - \mathbf{V}(\mathbf{x}, \mathbf{y}), \quad (10)$$

where  $\mathbf{F}$  is the rate of new infections from the susceptible population and  $\mathbf{V}$  is the rate of loss of infections due to recovery. They are

$$F_i = \beta m_i y_i \sum_j w_j m_j x_j, \quad V_i = \gamma x_i. \quad (11)$$

Consider the disease-free equilibrium, in which the whole population only contains susceptible individuals and its population density satisfies  $S(m, t) \equiv f(m)$ . Therefore, the disease-free equilibrium vectors  $\mathbf{x}^0, \mathbf{y}^0 \in \mathbb{R}^M$  satisfy  $x_i^0 = f(m_i)$  and  $y_i^0 = 0$ . We compute the Jacobi matrices of  $\mathbf{F}$  and  $\mathbf{V}$  with respect to  $\mathbf{x}$  at the disease-free equilibrium vectors  $\mathbf{x}^0, \mathbf{y}^0$  and obtain

$$\frac{\partial \mathbf{F}}{\partial \mathbf{x}}(\mathbf{x}^0, \mathbf{y}^0)_{ij} = \beta m_i y_i^0 m_j w_j, \quad \frac{\partial \mathbf{V}}{\partial \mathbf{x}}(\mathbf{x}^0, \mathbf{y}^0)_{ij} = \gamma \delta_{ij}, \quad (12)$$

where  $\delta_{ij}$  is the Kronecker delta function. We further compute the next-generation matrix

$$\frac{\partial \mathbf{F}}{\partial \mathbf{x}} \left( \frac{\partial \mathbf{V}}{\partial \mathbf{x}} \right)^{-1} = \frac{\beta}{\gamma} \begin{pmatrix} m_1 y_1^0 \\ \vdots \\ m_M y_M^0 \end{pmatrix} (m_1 w_1 \quad \cdots \quad m_M w_M)_j. \quad (13)$$

We compute the largest eigenvalue of the next-generation matrix and obtain the basic reproduction number  $\mathcal{R}_0 = \beta \sum_i w_i m_i^2 y_i^0 / \gamma$ . Notice that  $w_i$  are the weights of grid points in the numerical quadrature, so as the number of grids  $M$  goes to infinite,  $\mathcal{R}_0$  converges to the integral

$$\mathcal{R}_0 = \frac{\beta}{\gamma} \int_0^1 m^2 f(m) dm, \quad (14)$$

The above derivations can be made rigorous by using the Fréchet derivative with an appropriate definition of the function space. When the entire population has a constant mobility  $m_0$ , equivalent to the baseline SIRS model (2), the basic reproduction number in (14) is

$$\mathcal{R}_0 = \frac{\beta m_0^2}{\gamma} = \frac{\beta_{\text{eff}}}{\gamma}, \quad (15)$$

which is consistent with the results of the baseline SIRS model (2).

Let  $\text{var}(f)$  denote the variance of a mobility distribution  $f$ . Assuming that all distributions that have the same  $\mathcal{R}_0$ , from (14) we have

$$\langle mf \rangle^2 = \frac{\gamma}{\beta} \mathcal{R}_0 - \text{var}(f) \leq \frac{\gamma}{\beta} \mathcal{R}_0 = \langle mf_\delta \rangle^2. \quad (16)$$

where  $f_\delta$  is the Dirac delta distribution that has the same second-order moment as other distributions. Therefore, if we fix  $\mathcal{R}_0$ , the Dirac delta distribution  $f_\delta$  maximizes the mean mobility  $\langle mf \rangle$ . In practice, we often estimate  $\mathcal{R}_0$  by considering the early growth rate of cases and performing contact tracing studies, which is independent of model selection. As a result, using the value of  $\mathcal{R}_0$  to estimate the pandemic size with the baseline SIRS model tends to result in overestimation.

## 2.4 Mean mobility

Mobility plays a crucial role in the mobility-based compartmental models. We examine the mean mobility of three populations. We focus on the mobility-based SIR model, which is defined by the following equations

$$\frac{\partial}{\partial t} S(m, t) = -\beta \int_0^1 m m' S(m, t) I(m', t) dm', \quad (17a)$$

$$\frac{\partial}{\partial t} I(m, t) = \beta \int_0^1 m m' S(m, t) I(m', t) dm' - \gamma I(m, t) \quad (17b)$$

$$\frac{\partial}{\partial t} R(m, t) = \gamma I(m, t). \quad (17c)$$

We define  $Q_k^\varphi$  as the  $k$ th moment with respect to a nonnegative function  $\varphi(m, t)$ , which is

$$Q_k^\varphi(t) = \int_0^1 m^k \varphi(m, t) dm. \quad (18)$$

**Theorem 1.** *Let  $Q_k^S(t)$  be the  $k$ th moment of  $S(m, t)$  which is the solution of the mobility-based SIR model (17). If  $f$  is not a Dirac delta distribution, then for any  $k \geq 0$ , the ratio  $Q_{k+1}^S(t)/Q_k^S(t)$  strictly decreases with respect to  $t$ .*

*Proof.* We multiply  $m^k$  to (17a) and integrate  $m$  over  $[0, 1]$ . We obtain

$$\dot{Q}_k^S = -\beta Q_1^I Q_{k+1}^S, \quad \text{for all } k \geq 0. \quad (19)$$

By using (19), we obtain the time derivative of  $Q_{k+1}^S/Q_k^S$

$$\frac{d}{dt} \left( \frac{Q_{k+1}^S}{Q_k^S} \right) = \frac{1}{Q_k^S Q_k^S} \left( Q_k^S \dot{Q}_{k+1}^S - \dot{Q}_k^S Q_{k+1}^S \right) = -\frac{\beta Q_1^I}{Q_k^S Q_k^S} \left( Q_k^S Q_{k+2}^S - Q_{k+1}^S Q_{k+1}^S \right). \quad (20)$$

From Hölder's inequality, we know that

$$Q_k^S Q_{k+2}^S - Q_{k+1}^S Q_{k+1}^S > 0, \quad (21)$$

which implies that the time derivative in (20) is negative, so that  $Q_{k+1}^S(t)/Q_k^S(t)$  strictly decreases.  $\square$

For  $k = 0$ , the ratio in Theorem 1 simplifies to  $Q_1^S(t)/Q_0^S(t)$ , representing the mean mobility of the susceptible population. Thus, in the mobility-based SIR model (17), the mean mobility of the susceptible population decreases over time  $t$ . However, this monotonic property does not necessarily apply to the infected and recovered populations, as illustrated in Figure 4. In addition, if  $f$  is a Dirac delta distribution, then the mean mobility remains constant and is independent of time  $t$ .

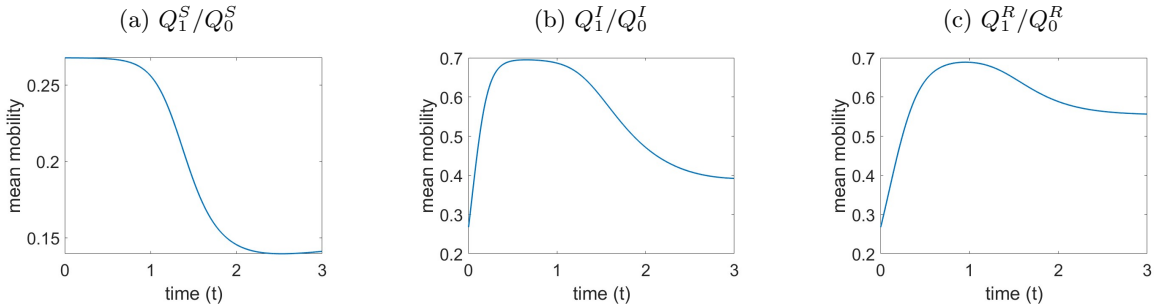


Figure 4: Time evolution of the mean mobility of three compartments in the mobility-based SIR model (17) with parameters  $\beta = 1.5$ ,  $\gamma = 0.13$ ,  $\varepsilon = 0.001$ ,  $I_0 = 1e-4$ , and  $f = f_1$  in (7). The mean mobility of the susceptible population is non-increasing, while the mean mobility of the infected and the recovered populations increases first and then decreases as time progresses.

## 2.5 Final pandemic size

The final pandemic size refers to the total number of individuals infected throughout an epidemic and is a crucial quantity to assess disease transmission dynamics. For the classical SIR model with a basic reproduction number  $\mathcal{R}_0$ , it is well known that the final pandemic size  $R_\infty$  satisfies the equation

$$R_\infty + \exp(-\mathcal{R}_0 R_\infty) = 1, \quad (22)$$

if the initial infected population  $I \approx 0$ . In the real world, the population exhibits heterogeneous mobility, with high-mobility individuals likely being infected first during the early pandemic stages. Once recovered, they provide some protection to low-mobility individuals. In practice,  $\mathcal{R}_0$  is typically estimated from the initial exponential growth rate, which is biased toward the infection rate of high-mobility individuals, thereby resulting in an overestimation of the final pandemic size. In this section, we derive the final pandemic size of the mobility-based SIR model (17) with the proportional initial condition (6). We rigorously demonstrate why the classic SIR model tends to overestimate the final size of pandemics, assuming the same  $\mathcal{R}_0$  as in the mobility-based SIR model.

**Theorem 2.** *Let  $R_\infty$  be the final pandemic size of the mobility-based SIR model (17) with the proportional initial condition (6). Assume  $I = 0 \approx 0$ , then  $R_\infty$  satisfies*

$$R_\infty + \langle f \exp(-\alpha m \beta / \gamma) \rangle = 1, \quad (23)$$

where  $\alpha$  is the solution of  $\alpha + \langle m f \exp(-\alpha m \beta / \gamma) \rangle = \langle m f \rangle$  on the interval  $[0, 1]$ .

*Proof.* By solving (2) for  $S(m, t)$ , we obtain that

$$S(m, t) = S(m, 0) \exp\left(-\frac{\beta}{\gamma} m \langle m R \rangle(t)\right). \quad (24)$$

We multiply the above equation by  $m$  and integrate it over  $m$ , then obtain

$$\langle m S \rangle(t) = \langle m S(m, 0) \exp\left(-\frac{\beta}{\gamma} m \langle m R \rangle(t)\right) \rangle. \quad (25)$$

Since  $I(m, t) \rightarrow 0$  as  $t \rightarrow \infty$ , we have

$$\langle m f \rangle - \langle m R \rangle(\infty) = \langle m S(m, 0) \exp\left(-\frac{\beta}{\gamma} m \langle m R \rangle(\infty)\right) \rangle. \quad (26)$$

We use the initial condition (6) and assume that  $S(m, 0) \approx f(m)$ , then  $\alpha = \langle m R \rangle(\infty)$  satisfies

$$\alpha + \langle m f \exp(-\alpha m \beta / \gamma) \rangle = \langle m f \rangle. \quad (27)$$

Integrating (24) and taking  $t$  to infinite, we obtain that  $R_\infty = \langle R \rangle(\infty)$  satisfies (23).  $\square$

Theorem 2 offers a method to compute the final pandemic size without the need to simulate the model (17) over time. The process involves first determining  $\alpha$  by finding the root of (27) within the interval  $[0, 1]$ . Once  $\alpha$  is obtained, we then solve (23) to find  $R_\infty$ . Additionally, once the parameters  $\beta$  and  $\gamma$  are fixed, the mobility distribution  $f(m)$  solely determines both the final pandemic size  $R_\infty$  and the basic reproduction number  $\mathcal{R}_0$  as given in (14). We will demonstrate in Theorem 3 that among all distributions that yield the same basic reproduction number, the Dirac delta distribution  $f_\delta$ , which corresponds to a homogeneous mobility of the population, maximizes the final pandemic size.

**Theorem 3.** *Let  $R_\infty$  and  $R_\infty^\delta$  be the final pandemic sizes associated with a distribution  $f$  and a Dirac delta distribution  $f_\delta$ , respectively. Suppose that  $f$  and  $f_\delta$  yield the same basic reproduction number  $\mathcal{R}_0$  (14), it holds that  $R_\infty \leq R_\infty^\delta$  with the equality occurring only if  $f = f_\delta$ .*

Theorem 2 provides an approach to compute the final pandemic size. We introduce another perspective to represent the final pandemic size to prove Theorem 3.

*Proof.* From (17), we have

$$\frac{dQ_0^S}{dt} = -\beta Q_1^S Q_1^I, \quad \frac{dQ_0^R}{dt} = \gamma Q_0^I, \quad t \in [0, \infty). \quad (28)$$

Since  $Q_0^R(t)$  monotonely increases with respect to  $t$ , so we have a one-to-one correspondence between  $Q_0^R(t)$  and  $t$ . Therefore, we can view all functions of  $t$  (including  $Q_0^S$ ) as a function of  $Q_0^R$ . Equation (28) becomes

$$\frac{dQ_0^S}{dQ_0^R} = -\frac{\beta}{\gamma} \tilde{H}(Q_0^R) Q_0^S, \quad Q_0^R \in [Q_0^R(0), Q_0^R(\infty)], \quad (29)$$

where

$$\tilde{H}(Q_0^R) = H(t) = \frac{Q_1^S(t) Q_1^I(t)}{Q_0^S(t) Q_0^I(t)}. \quad (30)$$

Recall that  $Q_0^R(0) = 0$ . We integrate (29) over the interval  $[0, Q_0^R(\infty)]$  and obtain

$$Q_0^S(\infty) = \exp\left(-\frac{\beta}{\gamma} \int_0^{Q_0^R(\infty)} \tilde{H}(\alpha) d\alpha\right). \quad (31)$$

Using  $\lim_{t \rightarrow \infty} Q_0^I(t) = 0$  and change of variable, we obtain

$$Q_0^R(\infty) + \exp\left(-\frac{\beta}{\gamma} \int_0^\infty H(t) dQ_0^R(t)\right) = 1. \quad (32)$$

As  $R_\infty^\delta$  satisfies

$$R_\infty^\delta + \exp(-\mathcal{R}_0 R_\infty^\delta) = 1, \quad (33)$$

it is sufficient to prove that

$$H(t) \leq \frac{\gamma}{\beta} \mathcal{R}_0 = \langle m^2 f \rangle, \quad \text{for all } t > 0, \quad (34)$$

where the equal sign holds only if  $f = f_\delta$ . It is not difficult to verify that the equality holds when  $f = f_\delta$ . We will assume that  $f \neq f_\delta$  and prove that  $H(t) < \langle m^2 f \rangle$  in the following proof.

From Theorem 1 for  $k = 1$  and Lemma 4, we have

$$\frac{Q_1^S(t)}{Q_0^S(t)} < \langle mf \rangle \quad \text{and} \quad \frac{Q_1^I(t)}{Q_0^I(t)} \leq \frac{\langle m^2 f \rangle}{\langle mf \rangle}, \quad \text{for all } t > 0. \quad (35)$$

Combining it with (30), we complete the proof.  $\square$

**Lemma 4.** *Let  $I(m, t)$  be the solution of the mobility-based SIR model (17) with the proportional initial condition (6). For all  $t > 0$ , it holds that*

$$\frac{Q_1^I(t)}{Q_0^I(t)} \leq \frac{\langle m^2 f \rangle}{\langle mf \rangle}, \quad (36)$$

*with equality occurring only if  $f$  is a Dirac delta distribution.*

*Proof.* If  $f$  is a Dirac delta distribution  $f(m) = \delta(m - m_0)$ , then both sides of (36) equal  $m_0$ . We assume that  $f$  is not a Dirac delta distribution in the following proof.

Using (17), we compute the time derivative of  $Q_1^I(t)/Q_0^I(t)$  and obtain

$$\frac{d}{dt} \left( \frac{Q_1^I}{Q_0^I} \right) = \frac{\beta Q_1^I Q_1^S}{Q_0^I} \left( \frac{Q_2^S}{Q_1^S} - \frac{Q_1^I}{Q_0^I} \right). \quad (37)$$

We denote the instants that  $\frac{d}{dt} (Q_1^I(t)/Q_0^I(t))$  changes its sign as  $t_k$  and partition the time interval  $(0, \infty)$  into open intervals  $\Omega_k$  with  $t_k$  as indicated in Figure 5.

Using the initial condition (6), we have

$$\frac{d}{dt} \left( \frac{Q_1^I}{Q_0^I} \right) (0) = \frac{\beta Q_1^I(0) Q_1^S(0)}{Q_0^I(0)} \left( \frac{\langle m^2 f \rangle}{\langle mf \rangle} - \langle mf \rangle \right) > 0, \quad (38)$$



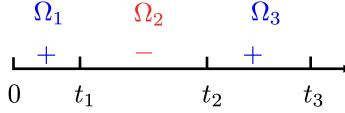


Figure 5: A partition of intervals due to the sign of (37).

which implies that  $\frac{d}{dt} (Q_1^I/Q_0^I)$  is nonnegative on the interval  $\Omega_1$ . Due to the smoothness, the signs of (37) interlace on  $\Omega_1, \Omega_2, \Omega_3, \dots$ .

If  $t \in \cup_{k=1}^{\infty} \overline{\Omega_{2k-1}}$ , then we know (37) is nonnegative, which implies that

$$\frac{Q_1^I(t)}{Q_0^I(t)} \leq \frac{Q_2^S(t)}{Q_1^S(t)} < \frac{Q_2^S(0)}{Q_1^S(0)} = \frac{\langle m^2 f \rangle}{\langle m f \rangle}, \quad (39)$$

where the second inequality uses Theorem 1 for the case  $k = 1$ . If  $t \in \cup_{k=1}^{\infty} \Omega_{2k}$  (supposing  $t \in \Omega_{2k}$ ), then  $Q_1^I(t)/Q_0^I(t)$  decreases with respect to  $t$  on the interval  $\Omega_{2k}$ . Due to continuity, we have

$$\frac{Q_1^I(t)}{Q_0^I(t)} \leq \frac{Q_1^I(t_{2k-1})}{Q_0^I(t_{2k-1})} < \frac{\langle m^2 f \rangle}{\langle m f \rangle}, \quad \text{for all } t \in \Omega_{2k-1}, \quad (40)$$

where the second inequality holds from (39). □

### 3 Learning the mobility distribution from data

Mobility holds critical significance in epidemic models as it directly influences the spread and dynamics of infectious diseases within populations. Understanding how people move between locations allows for more accurate predictions of disease transmission and enhances the precision of epidemic models to reflect real-world scenarios. However, the mobility of a population involves complex factors, including travel patterns, migration, and commuting, which are often impossible to measure directly in real-world situations. Realistically, the available data in epidemics is the number of infected individuals, which translates to the ratio of infected agents at time  $t$ :

$$Q_0^I(t) = \int_0^1 I(m, t) dm, \quad (41)$$

in the mobility-based SIRS model (4). In this section, we infer the mobility distribution  $f(m) \in \mathcal{L}^1(0, 1)$  from the time series of  $Q_0^I(t)$ , offering both a theoretical guarantee of unique inference and a machine-learning-based numerical approach.

#### 3.1 Theoretical guarantees

**Theorem 5.** *Let  $I(m, t)$  be the infected mobility distribution of the mobility-based SIRS model (4) with the initial condition (6), yielding the  $0$ th-order moment  $Q_0^I(t)$ . Assume that  $Q_0^I(m, t)$  is arbitrarily smooth (i.e.,  $Q_0^I \in \mathcal{C}^\infty(0, \infty)$ ) and all the parameters ( $I_0, \beta, \gamma$ , and  $\varepsilon$ ) are fixed and not equal to 0, then there is a one-to-one correspondence between  $f$  and  $Q_0^I$ .*

This theorem indicates that for any two different mobility distributions ( $f \neq \tilde{f}$ ), the corresponding time series of the infected numbers ( $Q_0^I$  and  $Q_0^{\tilde{I}}$ ) also differ. This implies that it is sufficient to infer  $f$  from  $I$  theoretically and this inference problem has a unique solution. We prove this theorem at the end of this subsection.

Recall the moment notation in (18). We multiply  $m^k$  to (4) and obtain the equations for moments

$$\frac{d}{dt}Q_k^S = -\beta Q_1^I Q_{k+1}^S + \varepsilon Q_k^R \quad (42a)$$

$$\frac{d}{dt}Q_k^I = \beta Q_1^I Q_{k+1}^S - \gamma Q_k^I \quad (42b)$$

$$\frac{d}{dt}Q_k^R = \gamma Q_k^I - \varepsilon Q_k^R. \quad (42c)$$

Consider another set of solutions  $\tilde{S}(m, t), \tilde{I}(m, t), \tilde{R}(m, t)$  of (4) with the initial condition proportional to  $\tilde{f}(m)$ .

**Lemma 6.** *The following three statements are equivalent:*

$$Q_k^S = Q_k^{\tilde{S}}, \quad Q_k^I = Q_k^{\tilde{I}}, \quad \text{and} \quad Q_k^R = Q_k^{\tilde{R}}. \quad (43)$$

*Proof.* We add (42a) and (42b) and obtain

$$\frac{d}{dt}Q_k^S + \frac{d}{dt}Q_k^I = \varepsilon Q_k^f - (\varepsilon + \gamma)Q_k^I - \varepsilon Q_k^S, \quad (44)$$

which utilizes the fact that  $Q_k^f = Q_k^S + Q_k^I + Q_k^R$ . Similarly, we have

$$\frac{d}{dt}Q_k^{\tilde{S}} + \frac{d}{dt}Q_k^{\tilde{I}} = \varepsilon Q_k^{\tilde{f}} - (\varepsilon + \gamma)Q_k^{\tilde{I}} - \varepsilon Q_k^{\tilde{S}}. \quad (45)$$

**Step 1.** We first show that  $Q_k^I = Q_k^{\tilde{I}}$  is equivalent to  $Q_k^S = Q_k^{\tilde{S}}$ . Suppose that  $Q_k^I = Q_k^{\tilde{I}}$ . We compute the difference between (44) and (45) and obtain

$$\frac{d}{dt}(Q_k^S - Q_k^{\tilde{S}}) = \varepsilon(Q_k^f - Q_k^{\tilde{f}}) - \varepsilon(Q_k^S - Q_k^{\tilde{S}}). \quad (46)$$

Since  $Q_k^I(0) = I_0 Q_k^f$  and  $Q_k^{\tilde{I}}(0) = I_0 Q_k^{\tilde{f}}$ , we use  $Q_k^I(0) = Q_k^{\tilde{I}}(0)$  and obtain

$$Q_k^f = Q_k^{\tilde{f}}, \quad Q_k^S(0) - Q_k^{\tilde{S}}(0) = S_0(Q_k^f - Q_k^{\tilde{f}}) = 0. \quad (47)$$

Therefore,  $e(t) = Q_k^S(t) - Q_k^{\tilde{S}}(t)$  satisfies a linear ODE

$$\frac{d}{dt}e(t) = -\varepsilon e(t), \quad e(0) = 0, \quad (48)$$

yielding  $e(t) = 0$  for all  $t \geq 0$ , so that  $Q_k^S = Q_k^{\tilde{S}}$ . Suppose that  $Q_k^S = Q_k^{\tilde{S}}$ . We use the similar idea as above and show  $e(t) = Q_k^I(t) - Q_k^{\tilde{I}}(t)$  satisfies

$$\frac{d}{dt}e(t) = -(\varepsilon + \gamma)e(t), \quad e(0) = 0, \quad (49)$$

which yields  $Q_k^I(t) = Q_k^{\tilde{I}}(t)$  for all  $t \geq 0$ .

**Step 2.** We then show that  $Q_k^I = Q_k^{\tilde{I}}$  is equivalent to  $Q_k^R = Q_k^{\tilde{R}}$ . Suppose that  $Q_k^R = Q_k^{\tilde{R}}$ . Therefore, we have  $dQ_k^R/dt = dQ_k^{\tilde{R}}/dt$ . From (42c), we have  $Q_k^I = Q_k^{\tilde{I}}$ . Suppose  $Q_k^I = Q_k^{\tilde{I}}$ . Using the similar idea as above, we have  $e(t) = Q_k^R - Q_k^{\tilde{R}}$  satisfies

$$\frac{d}{dt}e(t) = -\varepsilon e(t), \quad e(0) = 0, \quad (50)$$

implying that  $Q_k^R = Q_k^{\tilde{R}}$ .  $\square$

Theorem 5 and Lemma 6 indicate that there is a one-to-one correspondence between  $f$  and  $Q_0^S$  and that between  $f$  and  $Q_0^R$ . This implies that, alternatively, we can also infer the mobility distribution  $f$  from the time series of  $Q_0^S$  or  $Q_0^R$  if they are available and the inference problems yield unique solutions.

**Lemma 7.** *Let  $L$  be a positive integer and the moments satisfy*

$$\begin{aligned} \frac{d^\ell}{dt^\ell} Q_k^{S,I,R}(0) &= \frac{d^\ell}{dt^\ell} Q_k^{\tilde{S},\tilde{I},\tilde{R}}(0), \quad k = 0, 1, \dots, K-1-\ell, \\ \frac{d^\ell}{dt^\ell} Q_k^{S,I,R}(0) &\neq \frac{d^\ell}{dt^\ell} Q_k^{\tilde{S},\tilde{I},\tilde{R}}(0), \quad k = K-\ell. \end{aligned} \quad (51)$$

for  $\ell = 0, 1, \dots, L-1$ , then (51) also holds for  $\ell = L$ .

*Proof.* A direct computation yields

$$\frac{d^L}{dt^L} Q_k^I = \frac{d^{L-1}}{dt^{L-1}} (\beta Q_1^I Q_{k+1}^S - \gamma Q_k^I) = \beta \sum_{\alpha=0}^{L-1} C_{L-1}^\alpha \frac{d^\alpha}{dt^\alpha} Q_1^I \frac{d^{L-1-\alpha}}{dt^{L-1-\alpha}} Q_{k+1}^S - \gamma \frac{d^{L-1}}{dt^{L-1}} Q_k^I. \quad (52)$$

For  $k = 0, \dots, K-L-1$ , we use conditions in (51) and obtain

$$\frac{d^L}{dt^L} Q_k^I(0) = \frac{d^L}{dt^L} Q_k^{\tilde{I}}(0). \quad (53)$$

For  $k = K-L$ , we have

$$\begin{aligned} \frac{d^L}{dt^L} Q_{K-L}^I &= \beta \sum_{\alpha=0}^{L-1} C_{L-1}^\alpha \frac{d^\alpha}{dt^\alpha} Q_1^I \frac{d^{L-1-\alpha}}{dt^{L-1-\alpha}} Q_{K-L+1}^S - \gamma \frac{d^{L-1}}{dt^{L-1}} Q_{K-L}^I \\ &= \beta \sum_{\alpha=1}^{L-1} C_{L-1}^\alpha \frac{d^\alpha}{dt^\alpha} Q_1^I \frac{d^{L-1-\alpha}}{dt^{L-1-\alpha}} Q_{K-L+1}^S - \gamma \frac{d^{L-1}}{dt^{L-1}} Q_{K-L}^I + \beta Q_1^I \frac{d^{L-1}}{dt^{L-1}} Q_{K-L+1}^S. \end{aligned} \quad (54)$$

All paired moments from  $f$  and  $\tilde{f}$  are equal to each other at  $t = 0$  from (42), except for the last term since

$$\frac{d^{L-1}}{dt^{L-1}} Q_{K-L+1}^S(0) \neq \frac{d^{L-1}}{dt^{L-1}} Q_{K-L+1}^{\tilde{S}}(0). \quad (55)$$

We complete the proof for moments for the infected population. We repeat similar calculations for the moments of  $S$  and  $R$  and obtain the results.  $\square$

Now we prove Theorem 5.

*Proof.* We use the same moment notation (18). Since  $f \neq \tilde{f}$ , we can find a positive integer  $K$  such that

$$\begin{aligned} Q_k^f &= Q_k^{\tilde{f}}, \quad \text{for all } k = 0, 1, \dots, K-1, \\ Q_K^f &\neq Q_K^{\tilde{f}}. \end{aligned} \quad (56)$$

From the proportional initial condition (6), we have

$$\begin{aligned} Q_k^{S,I,R}(0) &= Q_k^{\tilde{S},\tilde{I},\tilde{R}}(0), \quad \text{for all } k = 0, 1, \dots, K-1, \\ Q_K^{S,I,R}(0) &\neq Q_K^{\tilde{S},\tilde{I},\tilde{R}}(0). \end{aligned} \quad (57)$$

We plug the initial values into (42) and obtain

$$\begin{aligned} \frac{d}{dt} Q_k^{S,I,R}(0) &= \frac{d}{dt} Q_k^{\tilde{S},\tilde{I},\tilde{R}}(0), \quad \text{for all } k = 0, 1, \dots, K-2, \\ \frac{d}{dt} Q_{K-1}^{S,I,R}(0) &\neq \frac{d}{dt} Q_{K-1}^{\tilde{S},\tilde{I},\tilde{R}}(0), \end{aligned} \quad (58)$$

where the last inequality for the recovered population also uses the facts that

$$Q_{K-1}^f = Q_{K-1}^S(0) + Q_{K-1}^I(0) + Q_{K-1}^R(0), \quad Q_{K-1}^{\bar{f}} = Q_{K-1}^{\bar{S}}(0) + Q_{K-1}^{\bar{I}}(0) + Q_{K-1}^{\bar{R}}(0). \quad (59)$$

Notice that (58) satisfies the conditions in Lemma 7 for  $L = 2$ . By induction, we know (51) hold for  $\ell = 2, 3, \dots, K$ . In particular, we use the inequality result in Lemma 7 for  $\ell = K$  and  $k = 0$  yielding

$$\frac{d^K}{dt^K} Q_0^I(0) \neq \frac{d^K}{dt^K} Q_0^{\bar{I}}(0). \quad (60)$$

Therefore, we have  $Q_0^I \neq Q_0^{\bar{I}}$  and the correspondence between  $f$  and  $Q_0^I$  is one-to-one.

□

### 3.2 Learning the mobility distribution using a neural-network framework

Mobility distribution significantly impacts the pandemic size and transmission. However, in reality, it is not feasible to directly measure the mobility density functions of different compartments during pandemics. Realistically, the available data in epidemics is often limited to the number of infected individuals. Theorem 5 suggests a one-to-one correspondence between the mobility distribution  $f(m)$  and the ratio of the infected population  $\langle I \rangle(t)$ . Thus, a natural approach is to infer the mobility distribution from the early-stage pandemic data to make accurate predictions for the future course of the pandemic. We propose a neural-network-based approach to learn the operator from the time-series  $\langle I \rangle(\cdot)$  to the mobility distribution  $f(\cdot)$ .

Assume that the pandemic data takes the form of  $\mathbf{I} = (\langle I \rangle(t_1), \dots, \langle I \rangle(t_{N_t}))^T$ , which is a time series of the ratio of the infected population at discrete time steps. We discretize  $\mathbf{f}$  using the discrete cosine transform (DCF) and denote the first  $N_f$  modes as  $\mathbf{f} = (\hat{f}_1, \dots, \hat{f}_{N_f})^T$ . We consider a feedforward neural network  $G_\theta$  to learn the mapping between  $\mathbf{I}$  and  $\mathbf{f}$ :

$$\mathbf{f} = G_\theta(\mathbf{I}). \quad (61)$$

We sample the mobility distribution  $f$  and obtain  $\langle I \rangle$  by simulating the mobility-based SIRS model (4) to form the training set. When using neural networks to learn unknown parameters or functions, it is crucial to sample a training set that encompasses a wide range of scenarios. In our context, this involves properly sampling the mobility distribution comprehensively and robustly. Since a Gaussian mixture model is a universal approximator of probability densities, we sample  $f$  by a Gaussian mixture with random coefficients. In particular, we let

$$f \propto \sum_{n=1}^3 r_n \mathcal{N}(\mu_n, \sigma_n^2), \quad (62)$$

where  $\mathcal{N}(\mu, \sigma^2)$  is the Gaussian density function with mean  $\mu$  and variance  $\sigma^2$  and  $r_n$ ,  $\mu_n$ , and  $\sigma_n$  are all uniformly distributed on  $[0, 1]$ ,  $[-0.2, 1.2]$ , and  $[0.01, 0.26]$ , respectively.

Suppose the dataset  $\mathcal{D}$  contains  $K$  pairs of  $\mathbf{I}$  and  $\mathbf{f}$ , which we obtain by discretizing  $\langle I \rangle$  and  $f$ . We parametrize  $G_\theta$  with a fully-connected feedforward neural network and minimize the loss function

$$L(\theta) = \frac{1}{K} \sum_{i=1}^K [G_\theta(\mathbf{I}_i) - \mathbf{f}_i]^2.$$

In our simulations, we use a six-layer-fully connected neural network. The width of layers are 128, 512, 512, 512, 128, and 32, respectively. Each layer includes a Sigmoid activation function and  $L^2$  regularization with a magnitude of 0.005. In addition, we choose  $N_f = 8$  and  $N_t = 101$ . For each training step, we sample a random batch from the training set and use the Adam optimizer with a learning rate of 0.0005 to minimize the loss function for each batch. We generate a training set of size 10,000 and train the neural network for 2,000 epochs. During each training epoch, we optimize the loss function using 1,562 batches with a batch size of 54.

### 3.3 Numerical results

To generate the testing data, we solve the mobility-based SIRS model (4) with the proportional initial condition (6). We integrate (4) over time using the fourth-order Runge–Kutta method. For the spatial domain, we employ uniform grids and compute the nonlocal integral using Simpson’s rule. The model parameters are  $\beta = 0.8, \varepsilon = 0.005, \gamma = 0.14$ , and  $I_0 = 1e-4$ .

Given the dataset  $\mathcal{D}$ , we obtain the mapping  $G_\theta$  by minimizing the loss function (3.2). To evaluate performance, we generate an additional six mobility distributions using (62) and simulate the corresponding time series of infected populations  $\mathbf{I}$  as inputs. Figure 6 shows a comparison between the learned mobility distributions and the ground truth. It is noteworthy that the testing inputs  $\mathbf{I}_i$  are not part of the original training set; however, the inferred mobility distributions are capable of capturing the trends of the ground truth and yield time series that closely match the ground truth.

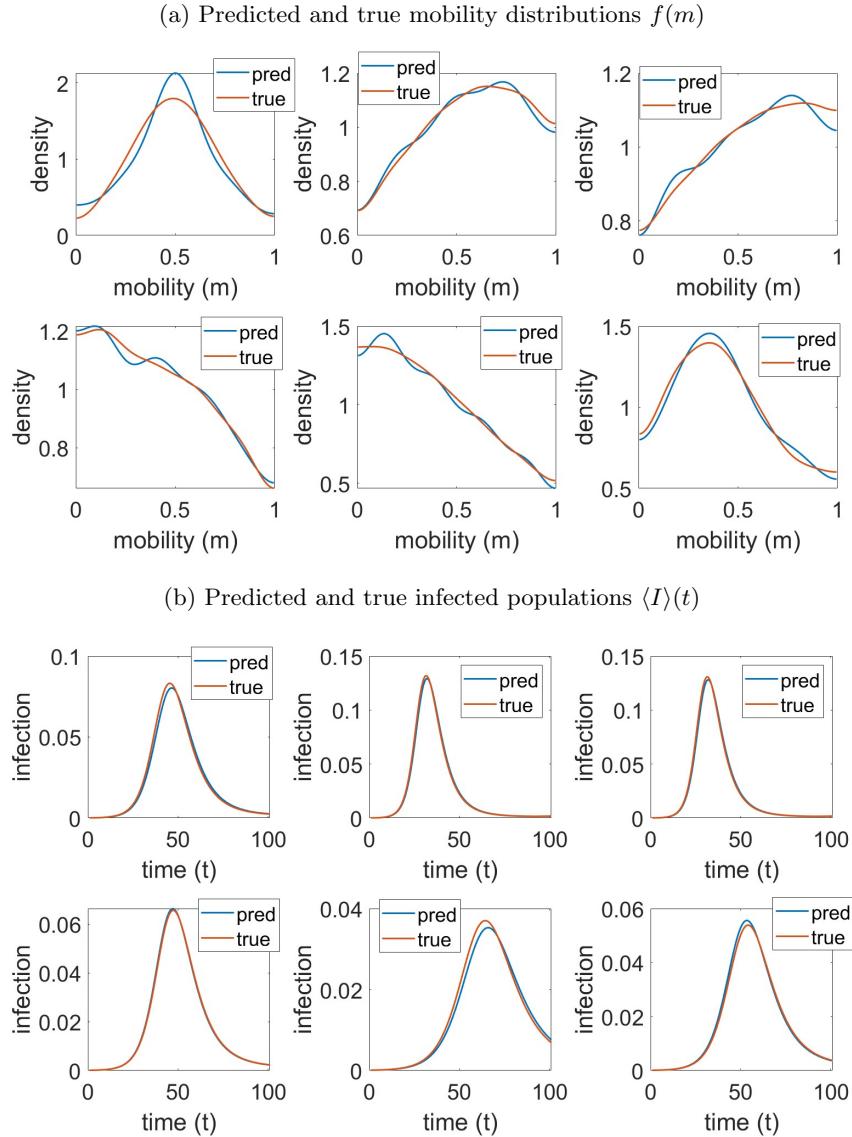


Figure 6: (a): A comparison between the predicted mobility distributions and the true distributions. (b): A comparison between the predicted and true  $\langle I \rangle(t)$ .

We analyze mobility distributions using real COVID-19 data, shown in Figure 7. From February 29th,

2020, to September 16th, 2020, covering the initial 200 days of our dataset, we examine the infection ratio between Massachusetts and New York. We calculate the total infected cases by summing daily new infections up to the current time, adjusted with a decaying prefactor to account for previously infected individuals. Specifically, we use

$$\langle I \rangle(t) = I_{\text{daily}}(t) + \exp(-1/\gamma)\langle I \rangle(t-1). \quad (63)$$

We recover the daily true case counts  $I_{\text{daily}}(t)$  from the death data and fit them with exponential growth for the first 30 days. The real data reflects a much smaller scale of disease transmission compared to the training set. To use the real data as input, we scale the input by a factor of 50. We show the resulting input data in Figure 7(a) and display the learned mobility distributions in Figure 7(b).

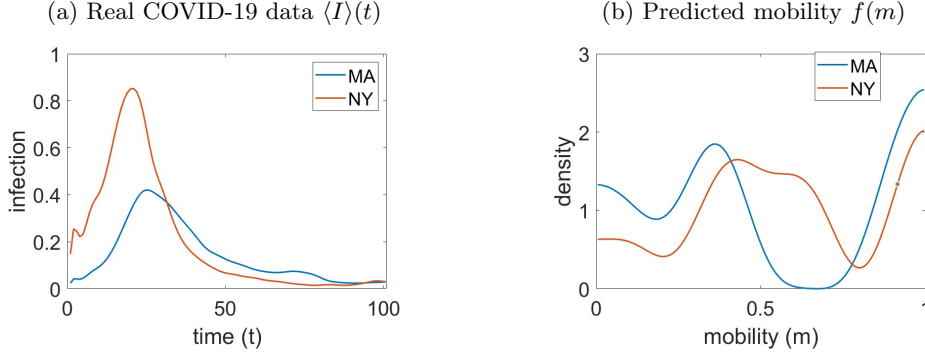


Figure 7: (a): The scaled ratio of COVID-19 infected cases during the initial wave in Massachusetts and New York from February 29th, 2020, to September 16th, 2020. (b): Inferred mobility distributions corresponding to the inputs in (a).

## 4 Conclusion and outlook

In this paper, we integrate social heterogeneity into compartmental models by introducing a mobility variable  $m$ , assuming it ranges from 0 to 1 for each individual. This approach represents the population in each compartment (susceptible, infected, recovered, etc.) as a density function over  $[0, 1]$ . Individuals with higher mobility are more prone to transmitting infectious diseases to others. The time evolution of population density for each compartment is described through an integro-differential equation.

We explore the key properties of the proposed mobility-based compartmental models crucial for epidemiological modeling, such as the basic reproduction number  $\mathcal{R}_0$ , final pandemic size, and mean mobility. The proposed mobility-based compartment models also effectively mitigate the overestimation problem inherent in many homogeneous compartmental models when estimating the final pandemic size. The basic reproduction rate  $\mathcal{R}_0$  is often estimated based on the initial growth rate of the infected population. In the early stages of a pandemic, individuals with higher mobility tend to get infected quickly, contributing to a higher  $\mathcal{R}_0$ . As the pandemic evolves, the recovered population with higher mobility can impart some degree of immunity to the broader population, particularly those with lower mobility. This process helps in mitigating the eventual final size of the pandemic. We rigorously demonstrate that under the same  $\mathcal{R}_0$ , the classical SIR model yields the largest final pandemic size. Numerical findings consistently indicate that a polarized mobility distribution typically results in a significantly smaller final pandemic size compared to the classical SIR model. Additionally, we establish a one-to-one correspondence between the time series of the total infected population and the mobility distribution, demonstrating that the mobility distribution can be practically inferred from infection data. We propose a deep learning-based algorithm for inferring the mobility distribution directly from the total infected population.

The primary objective of integrating mobility into compartmental disease models is to utilize the

mobility distribution as an intermediary connecting disease dynamics with social dynamics. Changes in public health policies and shifts in public opinion about infectious diseases influence disease spread by altering people’s mobility patterns. Moving forward, we plan to incorporate opinion dynamics into mobility-based compartmental models to explore the interplay between public opinion and disease transmission dynamics.

## Acknowledgement

YL and NJ are partially supported by NSF DMS-2108628.

## References

- [1] R. M. Anderson and R. M. May. *Infectious diseases of humans: Dynamics and control*. Oxford University Press, 1991.
- [2] S. Bansal, B. T. Grenfell, and L. A. Meyers. When individual behaviour matters: homogeneous and network models in epidemiology. *Journal of the Royal Society Interface*, 4(16):879–891, 2007.
- [3] G. Chowell, H. Nishiura, and L. M. Bettencourt. Comparative estimation of the reproduction number for pandemic influenza from daily case notification data. *Journal of the Royal Society Interface*, 4(12):155–166, 2007.
- [4] O. Diekmann, J. A. P. Heesterbeek, and J. A. Metz. On the definition and the computation of the basic reproduction ratio  $r_0$  in models for infectious diseases in heterogeneous populations. *Journal of Mathematical Biology*, 28:365–382, 1990.
- [5] M. Farboodi, G. Jarosch, and R. Shimer. Internal and external effects of social distancing in a pandemic. *Journal of Economic Theory*, 196:105293, 2021.
- [6] N. M. Ferguson, D. A. Cummings, S. Cauchemez, C. Fraser, S. Riley, A. Meeyai, S. Iamsirithaworn, and D. S. Burke. Strategies for containing an emerging influenza pandemic in southeast asia. *Nature*, 437(7056):209–214, 2005.
- [7] N. M. Ferguson, D. Laydon, G. Nedjati-Gilani, N. Imai, K. Ainslie, M. Baguelin, S. Bhatia, A. Boonyasiri, Z. Cucunubá, G. Cuomo-Dannenburg, et al. *Report 9: Impact of non-pharmaceutical interventions (NPIs) to reduce COVID19 mortality and healthcare demand*, volume 16. Imperial College London London, 2020.
- [8] S. Funk, M. Salathé, and V. A. Jansen. Modelling the influence of human behaviour on the spread of infectious diseases: a review. *Journal of the Royal Society Interface*, 7(50):1247–1256, 2010.
- [9] I. Holmdahl and C. Buckee. Wrong but useful—what covid-19 epidemiologic models can and cannot tell us. *New England Journal of Medicine*, 383(4):303–305, 2020.
- [10] M. J. Keeling and P. Rohani. *Modeling infectious diseases in humans and animals*. Princeton University Press, 2011.
- [11] W. O. Kermack and A. G. McKendrick. A contribution to the mathematical theory of epidemics. *Proceedings of the Royal Society of London. Series A, Containing Papers of A Mathematical and Physical Character*, 115(772):700–721, 1927.
- [12] J. O. Lloyd-Smith, S. J. Schreiber, P. E. Kopp, and W. M. Getz. Superspreading and the effect of individual variation on disease emergence. *Nature*, 438(7066):355–359, 2005.

- [13] H. Nishiura, G. Chowell, and C. Castillo-Chavez. Did modeling overestimate the transmission potential of pandemic (H1N1-2009)? Sample size estimation for post-epidemic seroepidemiological studies. *Plos one*, 6(3):e17908, 2011.
- [14] J. Shaman and A. Karspeck. Forecasting seasonal outbreaks of influenza. *Proceedings of the National Academy of Sciences*, 109(50):20425–20430, 2012.
- [15] A. Vaziry, T. Kolokolnikov, and P. Kevrekidis. Modelling of spatial infection spread through heterogeneous population: from lattice to partial differential equation models. *Royal Society Open Science*, 9(10):220064, 2022.
- [16] C. Viboud, K. Sun, R. Gaffey, M. Ajelli, L. Fumanelli, S. Merler, Q. Zhang, G. Chowell, L. Simonsen, A. Vespignani, et al. The RAPIDD ebola forecasting challenge: Synthesis and lessons learnt. *Epidemics*, 22:13–21, 2018.